Subexponential critical slowing-down at a Floquet time-crystal phase transition

Wenqian Zhang,[1,*] Yadong Wu,[1,2,3,*] Xingze Qiu,[1,2,3] Jue Nan,[1,2,3,†] and Xiaopeng Li[1,2,3,4,‡]

[1]*State Key Laboratory of Surface Physics, Key Laboratory of Micro and Nano Photonic Structures (MOE), and Department of Physics, Fudan University, Shanghai 200433, China*

[2]*Institute of Nanoelectronics and Quantum Computing, Fudan University, Shanghai 200433, China*

[3]*Shanghai Qi Zhi Institute, AI Tower, Xuhui District, Shanghai 200232, China*

[4]*Shanghai Artificial Intelligence Laboratory, Shanghai 200232, China*

(Received 18 January 2023; revised 30 May 2023; accepted 7 July 2023; published 21 July 2023)

Critical slowing-down (CSD) has been a trademark of critical dynamics for equilibrium phase transitions of a many-body system, where the relaxation time for the system to reach thermal equilibrium or the quantum ground state diverges with system size. The time-crystal phase transition has attracted much attention in recent years for it provides a scenario of phase transition of quantum dynamics, unlike conventional equilibrium phase transitions. Here, we study critical dynamics near the Floquet time-crystal phase transition. Its critical behavior is described by introducing a temporal coarse-grained correlation function, whose relaxation time diverges at the critical point revealing the CSD. This is demonstrated by investigating the Floquet dynamics of a one-dimensional disordered spin chain. Through finite-size scaling analysis, we show that the relaxation time has a universal subexponential scaling near the critical point, in sharp contrast to the standard power-law behavior for CSD in equilibrium phase transitions. This prediction can be readily tested in present quantum simulation experiments.

DOI: 10.1103/PhysRevB.108.014307

I. INTRODUCTION

Critical slowing-down (CSD) is a ubiquitous phenomenon near phase transitions reflecting a universal scaling relation between space and time, which emerges in a broad range of thermodynamic systems such as electronic materials [1–3], atomic quantum many-body systems [4,5], and even social science models [6,7]. It has been introduced in the Van Hove theory [8–10], describing the existence of zero-relaxation-rate modes at a second-order phase transition point. Its universality has been unveiled through a phenomenological approach proposing a dynamic scaling hypothesis [11–13], as later justified by the renormalization group (RG) theory of critical dynamics [14,15].

In recent years, the time crystal [16,17], a dynamical phase, has been attracting tremendous research interest. It has been established in theory that time crystals could be stabilized by long-range interactions [18], disorder-induced localization [19], or intricate nonlinear effects [20]. In experiments, time crystals have been found in quantum many-body dynamics of a variety of quantum systems such as trapped ions [21], superfluid helium [22,23], and cold atoms [24]. Despite the extensive studies on the time-crystal phases, the spontaneous symmetry breaking of the quantum dynamics near the phase transition remains less well understood. In particular, because the time-crystal phase transition is intrinsically a transition of dynamics, characterizing the CSD mechanism in this dynamical phase transition is fundamentally different from its equilibrium analog [25–27].

In this paper, we examine the spontaneous time-crystal phase transition in the Floquet dynamics of a disordered spin chain in one dimension (1D) [19,28]. The CSD is extended from the equilibrium setting to the dynamical phase transition by performing coarse graining in the time dimension. We find that the coarse-grained dynamics exhibits a diverging relaxation time near the dynamical phase transition. Based on the strong-disorder RG theory [15,29–32], we propose a finite-time–finite-size scaling form for the coarse-grained correlation. A large-scale numerical simulation for a system size up to 60 spins is carried out by mapping the spin chain to Majorana fermions. The numerical results show a nice data collapse on a universal curved surface. Our finite-size scaling analysis implies a subexponential slowing-down for the critical dynamics, unlike the standard CSD in equilibrium phase transitions.

II. MODEL

A prominent scenario to support the time-crystal phase is the spontaneous period doubling of Floquet quantum dynamics of 1D disordered spin chains, where heating effects caused by periodic driving are suppressed by many-body localization [33–35]. The quantum dynamics is described by Floquet operators [19,28,32,36,37],

$$\hat{U}_F = \exp\left[-it_2\sum_{j=1}^{L-1} J_j\hat{\sigma}_j^z\hat{\sigma}_{j+1}^z\right]\exp\left[-i\pi t_1 g\sum_{j=1}^{L}\hat{\sigma}_j^x\right]. \quad (1)$$

*These authors contributed equally to this work.
†juenan@fudan.edu.cn
‡xiaopeng_li@fudan.edu.cn

We take $t_1 = t_2 = 1/2$ and choose a lognormal distribution for the random Ising couplings (J_j). The couplings have a typical strength $J_{\rm typ}$ given by $\ln J_{\rm typ} = \frac{1}{L}\sum_j \ln J_j$, and their logarithms have a standard deviation σ_J. This model exhibits spontaneous Ising symmetry breaking and discrete time translation symmetry breaking in the parameter regime $1 - g < J_{\rm typ}/\pi < g \leqslant 1$ [19,28]. Throughout this paper, we take $J_{\rm typ} = 0.1\pi$ and $\sigma_J = 0.2\pi$, for which the critical point separating the symmetry-broken time-crystal phase and the symmetric phase is located at $g_c = 0.9$. Both of the phases are localized.

For each disorder configuration $\mathbf{J} \equiv (J_1, J_2, \ldots, J_{L-1})$, we perform coarse graining in the time direction by introducing

$$O(T, \mathbf{J}) = \frac{1}{LL_t}\left|\sum_j \sum_{n=T+1}^{T+L_t} \langle \hat{\sigma}_j^z(n, \mathbf{J})\hat{\sigma}_j^z(0)\rangle (-1)^n\right|, \quad (2)$$

where $\hat{\sigma}_j^z(n, \mathbf{J}) = (\hat{U}_F(\mathbf{J})^\dagger)^n \hat{\sigma}_j^z (\hat{U}_F(\mathbf{J}))^n$ and L_t is the averaged number of Floquet periods. With the lattice sites and multiple consecutive Floquet periods averaged over, the coarse-grained quantity $O(T, \mathbf{J})$ is introduced to diagnose the collective relaxation dynamics of the system that develops CSD at the phase transition.

In our numerical simulations, we choose a Néel state $|\uparrow\downarrow\uparrow\downarrow\cdots\rangle$ polarized in the z direction as the initial state of the Floquet evolution. Our main results, however, do not depend on this particular initial state (see Appendix C). The Floquet operator is mapped to dynamical evolution of noninteracting fermions by Jordan-Wigner transformation, by which the autocorrelation functions in Eq. (2) are constructed from the Pfaffian of the fermion system (Appendix A). In the symmetric paramagnetic phase, the spin polarization pattern in the initial state would relax during the Floquet time evolution and eventually disappears at the long-time limit, which corresponds to a vanishing autocorrelation, $O(T, \mathbf{J}) \to 0$ at large T. In the time-crystal phase, the initial spin polarization is retained in the quantum dynamics even at the long-time limit. This is characterized by a finite autocorrelation, $O(T, \mathbf{J}) \neq 0$. The relaxation dynamics of $O(T, \mathbf{J})$ closely resembles the order parameter of the Ising phase transition of equilibrium systems with a pinning field added to the boundary [38].

To extract the universal properties of the relaxation dynamics, we need to average over disorder configurations (different $\mathbf{J}$'s). It has been established by RG analysis that different ways of averaging disorder would produce different critical scaling [29,30]. Here we perform disorder averaging in two ways. One is arithmetic averaging and the other is geometric averaging, by which we obtain the mean value and the typical value

$$\overline{A}^{\rm mea} = \tfrac{1}{N_{\mathbf{J}}}\textstyle\sum_{k=1}^{N_{\mathbf{J}}} A(\mathbf{J}_k), \quad (3)$$

$$\overline{A}^{\rm typ} = \exp\left[\tfrac{1}{N_{\mathbf{J}}}\textstyle\sum_{k=1}^{N_{\mathbf{J}}} \ln A(\mathbf{J}_k)\right], \quad (4)$$

respectively, where $A(\mathbf{J}_k) = \langle \hat{A}\rangle$ is the quantum state expectation of a physical observable $\hat{A}$, k is the disorder index, and $N_{\mathbf{J}}$ is the number of disorder configurations.

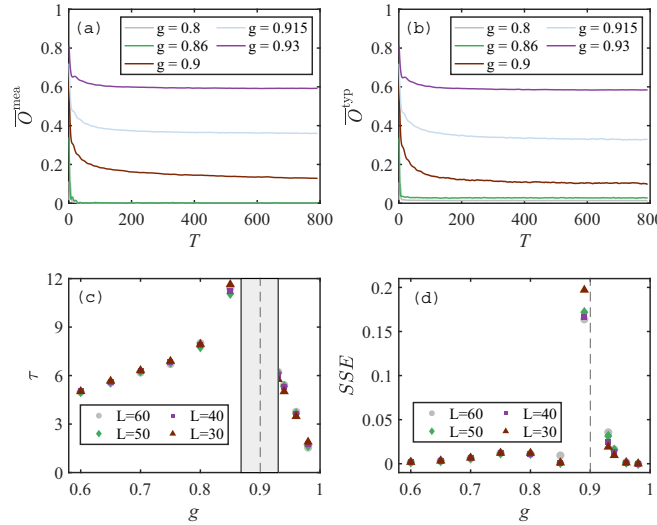

FIG. 1. The relaxation slowing-down at critical point $g_c = 0.9$. Dynamics of (a) mean and (b) typical correlation [Eq. (2)] with $L = 60$. Here, we average over $L_t = 10$ Floquet periods and 3000 disorder configurations. (c) The relaxation time obtained by fitting the relaxation dynamics to an exponential function. It systematically increases as the tuning parameter g approaches the critical point. The fitting fails in the shaded region, indicating nontrivial behavior of the critical dynamics. This regime is not sharply defined, but rather just marked there as a guide to the eye. (d) The sum of squares due to error (SSE) of the exponential fitting. The dashed lines mark the critical point.

III. RELAXATION ACROSS THE FLOQUET TIME-CRYSTAL PHASE TRANSITION

Figure 1 shows the relaxation dynamics. Away from the critical point, the system has a finite correlation length. It takes a finite amount of time for the system to dynamically relax. In the paramagnetic phase with $g < g_c$, we find that $\overline{O(T)}^{\rm mea}$ and $\overline{O(T)}^{\rm typ}$ quickly decay to zero after brief oscillations. The decay dynamics becomes relatively slower approaching the critical point.

While in the time-crystal phase with $g > g_c$, $\overline{O(T)}^{\rm mea}$ and $\overline{O(T)}^{\rm typ}$ also undergo swift decay before reaching their static value. At the critical point $g = g_c$, the relaxation dynamics develops an apparent long-tail behavior, which implies that the relaxation slows down dramatically.

From the relaxation dynamics, we extract the relaxation time τ by fitting the dynamics for different system sizes with an exponential function $\overline{O(T)}_{\rm fit} = a_1 e^{-T/\tau} + a_2$. The dynamics of $\overline{O(T)}^{\rm mea}$ fits well to the exponential function in the regime not too close to the critical point. Figures 1(c) and 1(d) show the extracted relaxation time and the fitting errors, respectively. We observe that the relaxation time τ rises up near the critical point on both sides of the phase transition. Deep in the time-crystal or the paramagnetic phase, the relaxation time is unaffected by the system size. In contrast, near the critical point, we find significant system-size dependence for the relaxation time. At the same time, the fitting error becomes substantially larger. The results with geometric average are qualitatively similar (see Appendix B). These observations

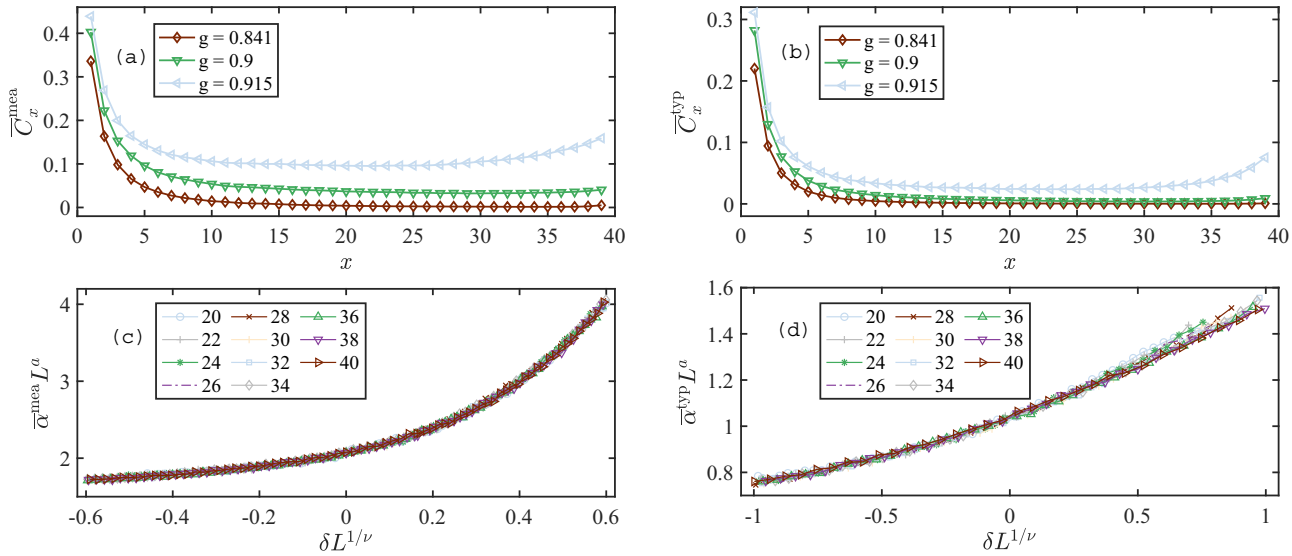

FIG. 2. Mean and typical correlation functions of Floquet eigenstates. (a) Mean and (b) typical spin correlation functions with system size $L = 40$ for the paramagnetic phase ($g = 0.841$), critical point ($g = 0.9$), and time-crystal phase ($g = 0.915$). Spin correlations are averaged over 2500 disorder configurations. (c) and (d) show the mean and typical maximum eigenvalue $\overline{\alpha}$ of the correlation function matrices, respectively, which acts as an order parameter reflecting the spatial long-range order. Finite-size scaling analysis has been performed on $\overline{\alpha}$. The correlation-length exponent ν, as defined by the correlation-length divergence at the critical point, $\xi \sim \delta^{-\nu}$, is 2.01 ± 0.02 for the mean case [Eq. (3)] and 1.12 ± 0.03 for the typical case [Eq. (4)]. The other exponent obtained for mean $\overline{\alpha}$ is $a = -0.170 \pm 0.002$ whereas for typical $\overline{\alpha}$, $a = -0.512 \pm 0.003$.

indicate that our introduced relaxation dynamics is indeed critical at the phase transition.

IV. FINITE-SIZE SCALING AND DYNAMICAL CRITICALITY

In order to systematically study the CSD of the relaxation near the phase transition, we analyze the Floquet dynamics with finite-size scaling theory. We first extract the ν exponents from the eigenstates of the effective Hamiltonian, which is defined by

$$\hat{U}_F(\mathbf{J}) = \exp[-i\hat{H}_{\rm eff}(\mathbf{J})]. \tag{5}$$

Figures 2(a) and 2(b) show the disorder-averaged correlation functions, $\overline{C_x}^{\rm mea}$ and $\overline{C_x}^{\rm typ}$, defined according to Eqs. (3) and (4) with $C_x^k = |\langle\phi_k|\hat{\sigma}_j^z\hat{\sigma}_{j+x}^z|\phi_k\rangle|$. Here, $|\phi_k\rangle$ denotes a random eigenstate in disorder configuration k, and we choose $j = \lceil (L-x)/2 \rceil$, $x = 1, 2, \ldots, L-1$, to minimize boundary effects. In the paramagnetic phase, the correlation function decays exponentially down to zero with a finite correlation length, whereas in the time-crystal phase, the correlation function saturates to a finite value at large distance. Near the critical point, the correlation length is comparable to the system size. The diverging behavior of the correlation length is reflected by the maximum eigenvalue (α_k) of the correlation matrix $\mathbf{C}^k$ with matrix elements $\mathbf{C}_{ij}^k = \langle\phi_k|\hat{\sigma}_i^z\hat{\sigma}_j^z|\phi_k\rangle$ [39]. Its disorder-averaged values, $\overline{\alpha}^{\rm mea}$ and $\overline{\alpha}^{\rm typ}$, are introduced correspondingly. For systems with long-range order, $\lim_{L\to\infty}\overline{\alpha}/L$ is finite, while $\lim_{L\to\infty}\overline{\alpha}/L \to 0$ for correlation functions that vanish at long distance. At the critical point, the $\overline{\alpha}$ value exhibits nontrivial scaling with the system size, reflecting the correlation-length criticality. With our numerical results, we find a reasonable data collapse [Figs. 2(c) and 2(d)] by taking a finite-size scaling ansatz [29–32],

$$\overline{\alpha} = L^{-a} f(\delta L^{1/\nu}), \tag{6}$$

with $\delta = [\ln(\pi g) - \ln(\pi - J_{\rm typ})]/\sigma_J^2$. For the arithmetic disorder average, we obtain $a = -0.170 \pm 0.002$ and $\nu = 2.01 \pm 0.02$. For the typical average, we obtain $a = -0.512 \pm 0.003$ and $\nu = 1.12 \pm 0.03$, having a sizable difference from the arithmetic average. These numerical results are consistent with disorder RG analysis at the infinite-randomness fixed point [30]. The typical correlation has a less divergent correlation length, which deviates substantially from the mean correlation because the latter receives a significant contribution from distant resonant pairs [29].

With the ν exponents obtained, we then perform the finite-size scaling analysis for the relaxation dynamics near the critical point. Although both the spatial correlation length ξ and the relaxation time τ have divergent behavior at the critical point, the disordered system lacks space-time symmetry: ξ and τ exhibit different scalings. Since the correlation length diverges at the critical point, it takes a divergent amount of time for the system to establish long-range spin correlations. It has been argued based on disorder RG theory that disordered systems obey an activated dynamic scaling $\ln\tau \sim \xi^b$ over a long time [40]. Since the dynamics of $\overline{O(T)}$ is analogous to the order parameter of an equilibrium system in the presence of pinning fields, we propose a two-variable scaling function [38,40]

$$\overline{O(T)} = L^{-\beta/\nu} G(L/\xi, \ln\tilde{T}/\ln\tilde{\tau}). \tag{7}$$

Here, we introduce the dimensionless time variables $\tilde{T}$ and $\tilde{\tau}$ defined as T/T_0 and τ/T_0, respectively, where T_0 is some

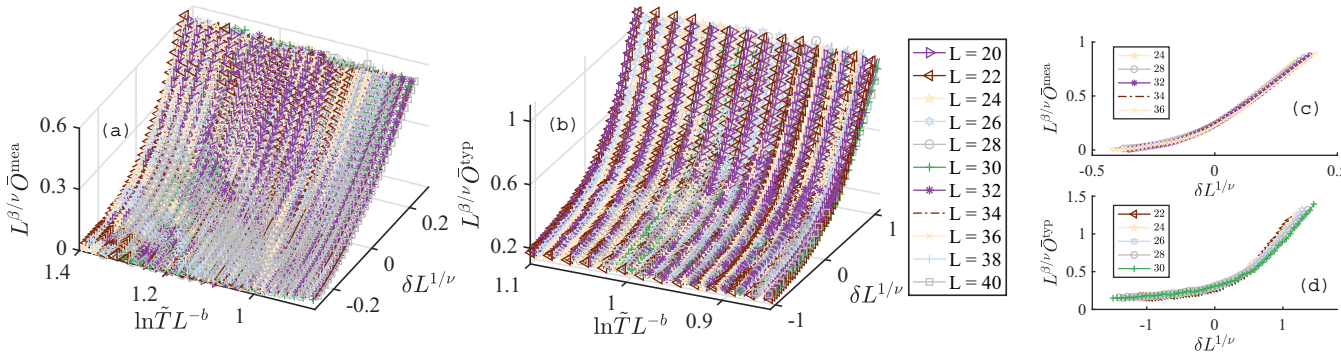

FIG. 3. The finite-size scaling results for the critical dynamics. (a) The finite-size scaling for the mean value of the correlation in Eq. (2). The fitting yields the exponents $b = 0.45 \pm 0.05$, $\beta = 0.32 \pm 0.18$, $g_c = 0.90$, and $T_0 = 2.03 \pm 0.28$. (b) The analysis for the typical value of the correlation, where we find $b = 0.54 \pm 0.09$, $\beta = 0.37 \pm 0.04$, $g_c = 0.90$, and $T_0 = 1.49 \pm 0.08$. The fitting error is obtained by bootstrapping. We take the ν exponents from the results in Fig. 2, to reduce the number of fitting parameters here. (c) and (d) Choosing the data for $\ln \tilde{T} L^{-b} \in [1, 1.02]$, cross sections of the collapsed surface are shown for the mean and typical values of the correlation. This demonstrates the high quality of the data collapse in the finite-size scaling analysis.

nonuniversal microscopic timescale analogous to nonuniversal microscopic length scales in equilibrium phase transitions [15]. Taking the activated dynamic scaling into account, the scaling function is rewritten as

$$\overline{O(T)} = L^{-\beta/\nu} F(\delta L^{1/\nu}, \ln \tilde{T}/L^b). \tag{8}$$

For the coarse graining, we average over multiple Floquet periods and choose $L_t = 10$ in Eq. (2), to filter out the short-time dynamics. To reduce the contribution of nonuniversal dynamics from state initialization, it is required to examine the long-time limit, with $T \gg L_t$. In our numerical simulations, we choose T in the range between 108 and 806 for finite-size scaling analysis. We sample 1500 disorder configurations, and the results for the finite-size scaling with the two variables in Eq. (8) are shown in Figs. 3(a) and 3(b) for mean and typical values, respectively. For both arithmetic and geometric averaging, the numerical data points from 11 system sizes ranging between $L = 20$ and $L = 40$ collapse onto a single smooth curved surface with the critical exponents $b = 0.45 \pm 0.05$ and $\beta = 0.32 \pm 0.18$ for the mean value and $b = 0.54 \pm 0.09$ and $\beta = 0.37 \pm 0.04$ for the typical value. The errors are obtained from bootstrapping [41]. The value of the exponent b which defines the property of dynamic scaling shows the subexponential nature of critical relaxation. More concretely, for either way of disorder averaging, the CSD in this dynamical phase transition takes an approximate form of

$$\tau \propto \exp[\sqrt{\delta^{-\nu}}]. \tag{9}$$

In the fitting we take the value of ν exponent determined through Eq. (6) to reduce the number of fitting variables here. The nonuniversal time scales are obtained to be $T_0 = 2.0 \pm 0.3$ for the mean value and $T_0 = 1.49 \pm 0.08$ for the typical value. Considering the evolution time we consider, this microscopic time scale is relatively small.

We further illustrate the quality of two-dimensional data collapse by cutting out a slice of data points, which are shown by line plots in Figs. 3(c) and 3(d). Here, we pick data points in a thin slice with $\ln \tilde{T} L^{-b} \in [1.00, 1.02]$ for both mean and typical correlations and plot $L^{\beta/\nu} \bar{O}$ as a function of $\delta L^{1/\nu}$. As shown in Figs. 3(c) and 3(d), the data points obtained from various system sizes consistently fall on a smooth curve taking the determined exponents, which yields a nice one-dimensional data collapse as widely used in analyzing equilibrium phase transitions [42]. This confirms the high quality of the two-dimensional data collapse and further justifies the scaling form assumed in Eq. (7). The analysis also verifies the critical exponents we determine to describe the CSD, and the resultant subexponential relation of the relaxation time with system size.

Although we do not have a rigorous proof for our results to apply to interacting systems (in the fermion language), it is reasonable to expect that our finding of subexponential critical slowing-down should apply beyond integrable models. The scaling function in Eq. (7) has been motivated by an infinite-randomness fixed point for general interacting disorder spin chains. This scaling function is confirmed in this paper by an integrable model, by which we are able to simulate large systems. It has been shown that weak interactions that respect the $\mathbb{Z}_2$ symmetry are irrelevant [32]. Whether the critical exponents may change when interactions are strong or break $\mathbb{Z}_2$ symmetry remains an outstanding open question. We would like to leave out this subtle issue for future studies because the numerical simulations for interacting systems are restricted to very small systems.

V. CONCLUSION

We find that the phenomenon of critical slowing-down, widely studied in equilibrium phase transitions, also carries over to the dynamical Floquet time-crystal phase transition. This is demonstrated by large-scale simulation of a disordered quantum spin chain. The critical slowing-down is described by introducing a temporal coarse-grained spin correlation, which can be measured directly in quantum simulation experiments. Through finite-size scaling analysis, we show that the relaxation time of the coarse-grained spin correlation has a universal divergence near the critical point. With both arithmetic and geometric averages, the relaxation time has an approximate subexponential form, which implies a drastic critical slowing-down of the time-crystal phase transition.

ACKNOWLEDGMENTS

We acknowledge Xiong-Jun Liu and W. Vincent Liu for helpful discussions. This work is supported by National Program on Key Basic Research Project of China (Grant No. 2021YFA1400900), National Natural Science Foundation of China (Grant No. 11934002), Shanghai Municipal Science and Technology Major Project (Grant No. 2019SHZDZX01), and Shanghai Science Foundation (Grant No. 21QA1400500).

APPENDIX A: FREE-FERMION METHOD

We consider a Floquet time-crystal model in a random spin chain in Eq. (1). In order to simulate larger systems, we map this model to a system of noninteracting fermions using Jordan-Wigner transformation. We break down the numerical procedure into four parts. For dynamics simulation, we compute the evolution for fermionic operators and map the initial state to its fermionic counterpart. The dynamics of the coarse-grained correlation $\overline{O(T)}$ can then be computed in the form of fermionic Pfaffians [43,44]. In terms of resolving eigenstates of the Floquet operator, we define a mapping between quadratic Hamiltonians and coefficient matrices that helps us compute the effective Hamiltonian defined in Eq. (5). By standard diagonalization of the effective Hamiltonian, we get the eigenstates of the Floquet operator. In the following, we discuss these step by step.

1. Floquet evolution in the fermionic basis

The Jordan-Wigner transformation reads

$$\hat{\sigma}_j^x = 2\hat{c}_j^\dagger \hat{c}_j - 1, \tag{A1}$$

$$\hat{\sigma}_j^y = \prod_{k=1}^{j-1}(1-2\hat{c}_k^\dagger\hat{c}_k)\hat{c}_j^\dagger + \prod_{k=1}^{j-1}(1-2\hat{c}_k^\dagger\hat{c}_k)\hat{c}_j, \tag{A2}$$

$$\hat{\sigma}_j^z = -i\prod_{k=1}^{j-1}(1-2\hat{c}_k^\dagger\hat{c}_k)\hat{c}_j^\dagger + i\prod_{k=1}^{j-1}(1-2\hat{c}_k^\dagger\hat{c}_k)\hat{c}_j, \tag{A3}$$

where $\hat{\sigma}_j^\alpha$ ($\alpha = x, y, z$) are spin-1/2 Pauli operators and $\hat{c}_j$ ($\hat{c}_j^\dagger$) represents the fermionic annihilation (creation) operator. Its inverse transformation is

$$\hat{c}_j = \frac{1}{2}\prod_{k=1}^{j-1}\big(-\hat{\sigma}_k^x\big)\big(\hat{\sigma}_j^y - i\hat{\sigma}_j^z\big) = \prod_{k=1}^{j-1}\big(-\hat{\sigma}_k^x\big)\hat{\sigma}_j^-, \tag{A4}$$

$$\hat{c}_j^\dagger = \frac{1}{2}\prod_{k=1}^{j-1}\big(-\hat{\sigma}_k^x\big)\big(\hat{\sigma}_j^y + i\hat{\sigma}_j^z\big) = \prod_{k=1}^{j-1}\big(-\hat{\sigma}_k^x\big)\hat{\sigma}_j^+. \tag{A5}$$

With these transformations, the evolved annihilation operator $\hat{c}_m$ ($1 < m < L$) after one Floquet period is

$$\begin{aligned}
\hat{U}_F^\dagger \hat{c}_m \hat{U}_F =& \hat{U}_F^\dagger \prod_{k=1}^{m-1}\big(-\hat{\sigma}_k^x\big)\hat{\sigma}_m^- \hat{U}_F = \frac{1}{2}\prod_{k=1}^{m-1}\big(-\hat{\sigma}_k^x\big)\hat{\sigma}_m^y\big[\cos(J_m)e^{-i\pi g\hat{\sigma}_m^x} - i\sin(J_m)\hat{\sigma}_m^z\hat{\sigma}_{m+1}^z e^{-i\pi g\hat{\sigma}_{m+1}^x}\big] \\
&- \frac{i}{2}\prod_{k=1}^{m-1}\big(-\hat{\sigma}_k^x\big)\hat{\sigma}_m^z\big[\cos(J_{m-1})e^{-i\pi g\hat{\sigma}_m^x} - i\sin(J_{m-1})\hat{\sigma}_{m-1}^z\hat{\sigma}_m^z e^{-i\pi g\hat{\sigma}_{m-1}^x}\big] \\
&= \frac{i}{2}\sin(J_m)e^{i\pi g}\hat{c}_{m+1}^\dagger - \frac{i}{2}\sin(J_m)e^{-i\pi g}\hat{c}_{m+1} \\
&+ \frac{1}{2}[\cos(J_m) - \cos(J_{m-1})]e^{i\pi g}\hat{c}_m^\dagger + \frac{1}{2}[\cos(J_{m-1}) + \cos(J_m)]e^{-i\pi g}\hat{c}_m \\
&- \frac{i}{2}\sin(J_{m-1})e^{i\pi g}\hat{c}_{m-1}^\dagger - \frac{i}{2}\sin(J_{m-1})e^{-i\pi g}\hat{c}_{m-1},
\end{aligned} \tag{A6}$$

where the Floquet operator $\hat{U}_F$ is defined in Eq. (1). For convenience we further introduce Majorana fermions through basis transformation

$$\hat{\gamma}_{2j-1} = -i(\hat{c}_j - \hat{c}_j^\dagger) \quad \text{and} \quad \hat{\gamma}_{2j} = \hat{c}_j + \hat{c}_j^\dagger. \tag{A7}$$

This transformation can be described by a transformation matrix U_C

$$(\hat{\gamma}_1\hat{\gamma}_2\cdots\hat{\gamma}_{2L-1}\hat{\gamma}_{2L})^T = U_C(\hat{c}_1\hat{c}_2\cdots\hat{c}_L\hat{c}_1^\dagger\cdots\hat{c}_L^\dagger)^T. \tag{A8}$$

In the Majorana basis, Eq. (A6) is rewritten as

$$\begin{aligned}
\hat{U}_F^\dagger\hat{\gamma}_{2m}\hat{U}_F =& \cos(J_m)\sin(\pi g)\hat{\gamma}_{2m-1} \\
&+ \cos(J_m)\cos(\pi g)\hat{\gamma}_{2m} \\
&+ \sin(J_m)\cos(\pi g)\hat{\gamma}_{2m+1} \\
&- \sin(J_m)\sin(\pi g)\hat{\gamma}_{2m+2},
\end{aligned} \tag{A9}$$

$$\begin{aligned}
\hat{U}_F^\dagger\hat{\gamma}_{2m+1}\hat{U}_F =& -\sin(J_m)\sin(\pi g)\hat{\gamma}_{2m-1} \\
&- \sin(J_m)\cos(\pi g)\hat{\gamma}_{2m} \\
&+ \cos(J_m)\cos(\pi g)\hat{\gamma}_{2m+1} \\
&- \cos(J_m)\sin(\pi g)\hat{\gamma}_{2m+2},
\end{aligned} \tag{A10}$$

where $1 \leqslant m \leqslant L-1$. For the boundaries ($m = 0$ and L), we have

$$\hat{\gamma}_1 = -\hat{\sigma}_1^z, \quad \hat{\gamma}_{2L} = -i\prod_{k=1}^{L}\big(-\hat{\sigma}_k^x\big)\hat{\sigma}_L^z. \tag{A11}$$

The evolution of operators $\hat{\gamma}_1$ and $\hat{\gamma}_{2L}$ can be computed with the form equations (A11)

$$\hat{U}_F^\dagger \hat{\gamma}_1 \hat{U}_F = \cos(\pi g)\hat{\gamma}_1 - \sin(\pi g)\hat{\gamma}_2,$$
$$\hat{U}_F^\dagger \hat{\gamma}_{2L} \hat{U}_F = \cos(\pi g)\hat{\gamma}_{2L} + \sin(\pi g)\hat{\gamma}_{2L-1}. \quad \text{(A12)}$$

In sum, after n Floquet periods of evolution, the evolved Majorana fermion $\hat{\gamma}_m(n)$ $(1 \leqslant m \leqslant 2L)$ can be expressed as

$$\hat{\gamma}_m(n) = (\hat{U}_F^\dagger)^n \hat{\gamma}_m(0)(\hat{U}_F)^n = [(V_F)^n \mathbf{\Gamma}(0)]_m, \quad \text{(A13)}$$

where the matrix elements of V_F are given in Eqs. (A9), (A10), and (A12). The vector $\mathbf{\Gamma}$ is defined as

$$\mathbf{\Gamma} = (\hat{\gamma}_1, \hat{\gamma}_2, \ldots, \hat{\gamma}_{2L})^T. \quad \text{(A14)}$$

From now on, the Floquet dynamics of the model will be described through V_F, as shown in Appendix A 3.

2. Mapping the initial Néel state to the respective fermionic state

To map the Néel state to the corresponding fermionic state, we choose a Hamiltonian $\hat{H}_s$ whose ground state is the Néel state

$$\hat{H}_s = \sum_{j=1}^{L-1} J_j \hat{\sigma}_j^z \hat{\sigma}_{j+1}^z. \quad \text{(A15)}$$

We would transform $\hat{H}_s$ into the fermionic basis $\hat{H}_f$ and map the fermionic ground state of $\hat{H}_f$ with the Néel state. Since Hamiltonian $\hat{H}_s$ has two degenerate ground states

$$|+\rangle = \tfrac{1}{\sqrt{2}}(|\uparrow\downarrow\uparrow\downarrow\cdots\rangle + |\downarrow\uparrow\downarrow\uparrow\cdots\rangle),$$
$$|-\rangle = \tfrac{1}{\sqrt{2}}(|\uparrow\downarrow\uparrow\downarrow\cdots\rangle - |\downarrow\uparrow\downarrow\uparrow\cdots\rangle)$$

and the Néel state is the superposition of these two Ising symmetric ground states

$$|\uparrow\downarrow\uparrow\downarrow\cdots\rangle = \frac{1}{\sqrt{2}}(|+\rangle + |-\rangle),$$

we need to map both $|+\rangle$ and $|-\rangle$ to fermionic states before properly mapping the Néel state. First we transform $\hat{H}_s$ into its fermionic counterpart using Eqs. (A1)–(A3)

$$\hat{H}_f = \sum_j J_j(-\hat{c}_j^\dagger \hat{c}_{j+1}^\dagger + \hat{c}_j^\dagger \hat{c}_{j+1} - \hat{c}_j \hat{c}_{j+1}^\dagger + \hat{c}_j \hat{c}_{j+1}). \quad \text{(A16)}$$

We further diagonalize $\hat{H}_f$ through Bogoliubov transformation with the transformation matrix U_B

$$(\hat{\eta}_0 \hat{\eta}_1 \cdots \hat{\eta}_{L_1} \hat{\eta}_0^\dagger \cdots \hat{\eta}_{L-1}^\dagger)^T = U_B(\hat{c}_1 \hat{c}_2 \cdots \hat{c}_1^\dagger \cdots \hat{c}_L^\dagger)^T. \quad \text{(A17)}$$

This gives the diagonalized Hamiltonian $\hat{H}_{fd} = \sum_k \epsilon_k \hat{\eta}_k^\dagger \hat{\eta}_k$, where a constant has been neglected. The degenerate ground states in $\hat{H}_s$ [Eq. (A15)] guarantee the existence of a zero mode with $\epsilon_0 = 0$ in $\hat{H}_{fd}$. The vacuum state $|0\rangle$ is a ground state and together with $|1\rangle = \hat{\eta}_0^\dagger|0\rangle$ can be matched with the degenerate ground states $|+\rangle$ and $|-\rangle$ of the spin model

$$|+\rangle = \alpha_+|0\rangle + \beta_+|1\rangle, \quad |-\rangle = \alpha_-|0\rangle + \beta_-|1\rangle. \quad \text{(A18)}$$

The objective of mapping the Néel state $|\uparrow\downarrow\uparrow\cdots\uparrow\downarrow\rangle$ to a fermionic state can thus be achieved by determining the coefficients in Eq. (A18). Here, $|0\rangle$ is chosen to be a parity-even vacuum. The spin and fermionic representations of the parity operator are shown below. Judging by the fermionic representation, we can always redefine $\hat{\eta}_0$ to satisfy the requirement of even parity. Besides the parity operator, a boundary spin operator is also considered in order to give coefficients α_+, β_+, α_-, and β_-. The first operator we choose is the parity operator. We define it in the spin basis and transform it into its fermionic counterpart using Eqs. (A1)–(A3)

$$\hat{P}_x \equiv \hat{\sigma}_1^x \hat{\sigma}_2^x \cdots \hat{\sigma}_L^x = (-i)^L \hat{\gamma}_1 \hat{\gamma}_2 \cdots \hat{\gamma}_{2L}. \quad \text{(A19)}$$

The spin states $\{|+\rangle, |-\rangle\}$ constitute a two-dimensional Hilbert subspace. We construct the representation matrix by computing all its elements $\langle \pm|\hat{P}_x|\pm\rangle$. Thus the representation matrix is

$$P_x^{(S)} = \begin{pmatrix} 1 & 0 \\ 0 & -1 \end{pmatrix}$$

in the spin basis $(|+\rangle, |-\rangle)^T$. Now we elaborate on the fermionic representation. We always invoke Wick's theorem in computing the expectation value of a string of noninteracting fermionic operators in the vacuum state $|0\rangle$. As an example, the expectation value of the parity operator can be written in the form of a Pfaffian

$$\langle 0|\hat{P}_x|0\rangle = (-i)^L \langle 0|\hat{\gamma}_1 \hat{\gamma}_2 \cdots \hat{\gamma}_{2L}|0\rangle = \mathrm{Pf}(G), \quad \text{(A20)}$$

where $\mathrm{Pf}(G)$ denotes the Pfaffian of a $2L \times 2L$ antisymmetric matrix G. The elements of matrix G are defined as

$$G_{ij} \equiv \begin{cases} -i\langle 0|\hat{\gamma}_i \hat{\gamma}_j|0\rangle, & i \neq j \\ 0, & i = j. \end{cases} \quad \text{(A21)}$$

The expectation value of a quadratic Majorana fermionic operator can be computed through operator transformation. Combining Eqs. (A8) and (A17), we have the transformation U_G between the Majorana fermionic basis and the quasiparticle basis

$$(\hat{\gamma}_1 \hat{\gamma}_2 \cdots \hat{\gamma}_{2L})^T = U_C U_B^\dagger (\hat{\eta}_0 \hat{\eta}_1 \cdots \hat{\eta}_{L-1} \hat{\eta}_0^\dagger \hat{\eta}_1^\dagger \cdots \hat{\eta}_{L-1}^\dagger)^T$$
$$\equiv U_G (\hat{\eta}_0 \hat{\eta}_1 \cdots \hat{\eta}_{L-1} \hat{\eta}_0^\dagger \hat{\eta}_1^\dagger \cdots \hat{\eta}_{L-1}^\dagger)^T.$$

For $i \neq j$,

$$\langle 0|\hat{\gamma}_i \hat{\gamma}_j|0\rangle = \sum_{l,k=1}^{L} (U_G)_{il} \langle 0|\hat{\eta}_{l-1} \hat{\eta}_{k-1}^\dagger|0\rangle (U_G^\dagger)_{kj}$$
$$\equiv (U_G P U_G^\dagger)_{ij},$$

where the $2L \times 2L$ diagonal matrix $P = \left(\begin{smallmatrix} I_L & 0_L \\ 0_L & 0_L \end{smallmatrix}\right)$, with I_L denoting an identity matrix. Note that the odd number of fermion operators gives a vanishing expectation value under the vacuum state. This means $\langle 1|\hat{P}_x|0\rangle = \langle 0|\hat{P}_x|1\rangle = 0$. Finally, for $|1\rangle = \eta_0^\dagger|0\rangle$, ground state $|1\rangle$ always has different parity from $|0\rangle$.

By now, we have arrived at the representation matrix of the parity operator

$$P_x^{(F)} = \begin{pmatrix} \mathrm{Pf}(G) & 0 \\ 0 & -\mathrm{Pf(G)} \end{pmatrix}$$

in the fermionic basis $(|0\rangle, |1\rangle)^T$. Having chosen the parity-even vacuum as $|0\rangle$, the representation matrices have $P_x^{(F)} = P_x^{(S)}$ with $\mathrm{Pf}(G) = 1$. The relation of Eq. (A18) can be simplified to $\alpha_+ = 1, \alpha_- = \beta_+ = 0, |\beta_-| = 1$.

We next turn to operator $\hat{\sigma}_1^z$ to determine β_-. We denote this operator $\hat{E}_z$ and then map it to Majorana fermions

$$\hat{E}_z \equiv \hat{\sigma}_1^z = -\hat{\gamma}_1. \tag{A22}$$

The representation of $\hat{E}_z$ is always easy to compute in the spin basis $(|+\rangle, |-\rangle)^T$

$$E_z^{(S)} = \begin{pmatrix} 0 & 1 \\ 1 & 0 \end{pmatrix}. \tag{A23}$$

The elements of the representation matrix of the $\hat{E}_z$ in the fermionic basis $(|0\rangle, |1\rangle)^T$ are

$$\begin{aligned} &\langle 0| - \hat{\gamma}_1 |0\rangle = \langle 1| - \hat{\gamma}_1 |1\rangle = 0, \\ &\langle 1| - \hat{\gamma}_1 |0\rangle = -\langle 0|\hat{\eta}_0 \hat{\gamma}_1 |0\rangle = -C_1^*, \\ &\langle 0| - \hat{\gamma}_1 |1\rangle = -\langle 0|\hat{\gamma}_1 \hat{\eta}_0^\dagger |0\rangle = -C_1, \end{aligned} \tag{A24}$$

where C_1 is the first element of vector $\boldsymbol{C}$ defined as

$$C_j \equiv \langle 0|\hat{\gamma}_j \hat{\eta}_0^\dagger |0\rangle. \tag{A25}$$

The computation of $\boldsymbol{C}$ is similar to the matrix G, where we invoke the transformation of Majorana fermions

$$C_j = \langle 0|\hat{\gamma}_j \hat{\eta}_0^\dagger |0\rangle = \sum_{k=1}^{L} (U_G)_{jk} \langle 0|\hat{\eta}_{k-1} \hat{\eta}_0^\dagger |0\rangle = (U_G)_{j1}.$$

Thus $\boldsymbol{C}$ is the first column of the matrix U_G. Now that Eq. (A24) gives the representation of the edge operator

$$E_z^{(F)} = \begin{pmatrix} 0 & -C_1 \\ -C_1^* & 0 \end{pmatrix}, \tag{A26}$$

we can use the transformation between the two bases [Eq. (A18)] to resolve the undetermined coefficient. The two representation equations (A23) and (A26) have the relation

$$A^\dagger E_z^{(S)} A = E_z^{(F)},$$

with the unitary $A = \left(\begin{smallmatrix} 1 & 0 \\ 0 & \beta_- \end{smallmatrix}\right)$, which gives

$$\beta_- = -1/C_1. \tag{A27}$$

In sum, we can now map the Néel state to a fermionic state

$$|\uparrow\downarrow\uparrow\downarrow\cdots\rangle = \frac{1}{\sqrt{2}}(|+\rangle + |-\rangle) = \frac{1}{\sqrt{2}}\left(|0\rangle - \frac{1}{C_1}|1\rangle\right). \tag{A28}$$

In principle, once we map a spin state $|+\rangle$ to a fermionic state $|0\rangle$, for any designated state indexed by k, we can find an operator $\hat{O}^k$

$$\hat{O}_s^k |+\rangle \Longleftrightarrow \hat{O}_f^k |0\rangle,$$

where the spin operator $\hat{O}_s^k$ is related to the fermionic operator $\hat{O}_f$ by Jordan-Wigner transformation [Eqs. (A1)–(A3)].

3. Dynamics computation of a local spin operator

In the main text, we choose the Néel state $|\psi\rangle = |\uparrow\downarrow\uparrow\downarrow\cdots\rangle$ as the initial state. This product state on the z axis simplifies the computation of the autocorrelation operator $\hat{\sigma}_j^z(n)\hat{\sigma}_j^z(0)$ into computing the expectation value of operator $\hat{\sigma}_j^z$, which composes the coarse-grained order parameter in Eq. (2)

$$\langle\psi|\hat{\sigma}_j^z(n)|\psi\rangle = -\mathrm{Re}\big(\langle 0|\hat{\sigma}_j^z(n)|1\rangle / C_1\big).$$

Here, we have used the result of Eq. (A28). For $1 \leqslant j \leqslant L$, we map

$$\begin{aligned} \langle 0|\hat{\sigma}_j^z(n)|1\rangle &= -(i)^{j-1}\langle 0|\hat{\gamma}_1(n)\hat{\gamma}_2(n)\cdots\hat{\gamma}_{2j-1}(n)\hat{\eta}_0^\dagger(0)|0\rangle \\ &= (i)^{j+1}\mathrm{Pf}(M^j(n)), \end{aligned}$$

where we similarly construct a $2j \times 2j$ antisymmetric matrix $M^j(n)$ [43]

$$M^j(n) = \begin{pmatrix} iG^j(n) & \boldsymbol{C}^j(n) \\ -\boldsymbol{C}^j(n)^T & 0 \end{pmatrix}. \tag{A29}$$

Here, the vector $\boldsymbol{C}^j(n)$ and matrix $G^j(n)$ are sections of the larger time-dependent $\boldsymbol{C}(n)$ and $G(n)$ whose initial values are defined as Eqs. (A25) and (A21), respectively. Using the evolution of the Majorana fermions in Eq. (A13), the vector element $C(n)_j$ is

$$\begin{aligned} C(n)_j &= \langle 0|\hat{\gamma}_j(n)\hat{\eta}_0^\dagger(0)|0\rangle = \sum_{k=1}^{2L} [(V_F)^n]_{jk}\langle 0|\hat{\gamma}_k(0)\hat{\eta}_0^\dagger(0)|0\rangle \\ &= \sum_{k=1}^{2L} [(V_F)^n]_{jk} C_k(0). \end{aligned} \tag{A30}$$

Thus the effect of evolution of vector $\boldsymbol{C}$ is $\boldsymbol{C}(n) = (V_F)^n\boldsymbol{C}(0)$. In a similar way it can be shown that the time-dependent matrix $G(n) = (V_F)^n G(0)(V_F^\dagger)^n$. Computing the first $2j-1$ elements of $\boldsymbol{C}(n)$ gives $\boldsymbol{C}^j(n)$, while computing the first $2j-1$ rows and first $2j-1$ columns of $G(n)$ gives $G^j(n)$.

4. Effective Hamiltonian of the Floquet operator

The eigenstates of the Floquet unitary $\hat{U}_F$ can be achieved by first computing its effective Hamiltonian. Defined by $\exp(-i\hat{H}_{\mathrm{eff}}) \equiv \hat{U}_F$ [Eq. (5)], it is easier to cope with the effective Hamiltonian in the Majorana fermionic basis. From Eqs. (A1)–(A3) and (A7), we transform the binary Hamiltonian into

$$\hat{H}(t) = \begin{cases} \hat{H}_1 \equiv -i\pi g \sum_j \gamma_{2j-1}\gamma_{2j}, & 0 \leqslant t < t_1 \\ \hat{H}_2 \equiv i\sum_j J_j \gamma_{2j}\gamma_{2j+1}, & t_1 \leqslant t < t_1 + t_2. \end{cases} \tag{A31}$$

For an operator $\hat{B}$ that is quadratic in $\{\hat{\gamma}_j\}$, we define matrix $\tilde{B}$ by

$$\hat{B} = \frac{1}{4}\sum_{ij}(\tilde{B})_{ij}\hat{\gamma}_i\hat{\gamma}_j.$$

The mapping from the matrix $\tilde{B}$ to the operator $\hat{B}$ is denoted as $\mathcal{T}$

$$\mathcal{T}(\tilde{B}) = \hat{B}.$$

The mapping has the property [45]

$$[\mathcal{T}(\tilde{H}_1), \mathcal{T}(\tilde{H}_2)] = \mathcal{T}([\tilde{H}_1, \tilde{H}_2]).$$

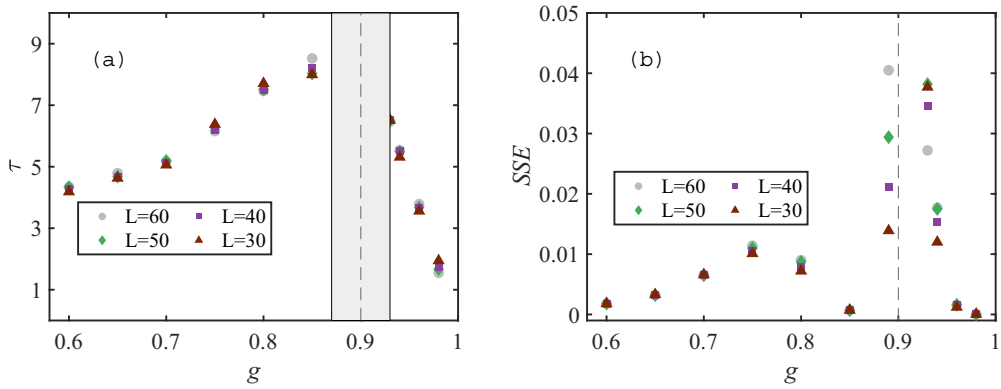

FIG. 4. Extracting relaxation time τ from the dynamics of the typical order parameter shown in Fig. 1(b). (a) System size has a negligible impact on τ away from the critical point. The relaxation time increases close to the critical point $g_c = 0.9$. The shaded region denotes the area where exponential fitting is deemed not appropriate. (b) The sum of squares due to error (SSE) of the exponential fitting shows a drastic increase near the critical point. The dashed lines mark the critical point.

This property gives us the matrix representation of the effective Hamiltonian [45]

$$\exp(-it_2\hat{H}_2)\exp(-it_1\hat{H}_1) = \exp[-i(t_1+t_2)\hat{H}_{\text{eff}}]$$
$$\Rightarrow \exp(-it_2\tilde{H}_2)\exp(-it_1\tilde{H}_1) = \exp[-i(t_1+t_2)\tilde{H}_{\text{eff}}].$$

The effective Hamiltonian is thus $\hat{H}_{\text{eff}} = \frac{1}{4}\mathbf{\Gamma}^\dagger \tilde{H}_{\text{eff}}\mathbf{\Gamma}$, with $\mathbf{\Gamma}$ defined in Eq. (A14). The eigenstates of the effective Hamiltonian, computed by standard diagonalization, are also the eigenstates of the Floquet operator.

APPENDIX B: RELAXATION TIME FOR TYPICAL CORRELATIONS

The relaxation time τ for $\overline{O(T)}^{\text{mea}}$ is shown in the main text. We use the dynamics $\overline{O(T)}^{\text{mea}}$ with $T \in [0, T_{\text{end}}]$, where $T_{\text{end}} = 790$, to perform the fitting. Here we show τ for the typical dynamics $\overline{O(T)}^{\text{typ}}$ [Fig. 1(b)] adopting the fitting function $\overline{O(T)}_{\text{fit}} = a_1 \exp(-T/\tau) + a_2$. The results are shown in Fig. 4(a). Similar to the mean case, the relaxation time τ increases from both sides of the critical point and is insensitive to the system size away from the transition point. The fitting is deemed inappropriate in the shaded region near the critical point. Corresponding fitting errors are shown in Fig. 4(b).

APPENDIX C: CRITICAL SLOWING-DOWN FOR RANDOM INITIAL STATES

We choose a Néel state as the initial state in the main text so that scaling-up the system size of the initial state comes naturally. The properties of critical dynamics, however, are generic and should not depend on the specific initial state. In Fig. 5, under a random product state in the z direction we show the mean and typical dynamics of coarse-grained correlations with $L = 60$. Averaged over 2000 disorder configurations, we find that a random state gives a smaller steady amplitude than the Néel state in the time-crystal phase [Figs. 1(a) and

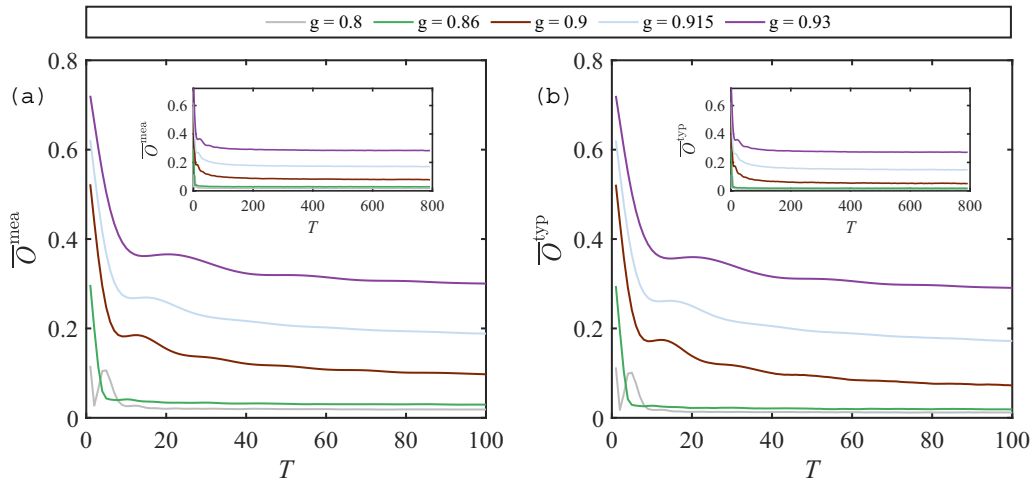

FIG. 5. The phenomenon of CSD is generic to a random initial state for (a) mean and (b) typical correlations. The random product state $|\psi\rangle = |s_1 s_2 \cdots s_{60}\rangle$, where $s_i \in \{\uparrow, \downarrow\}$. The insets show the long-time dynamics.

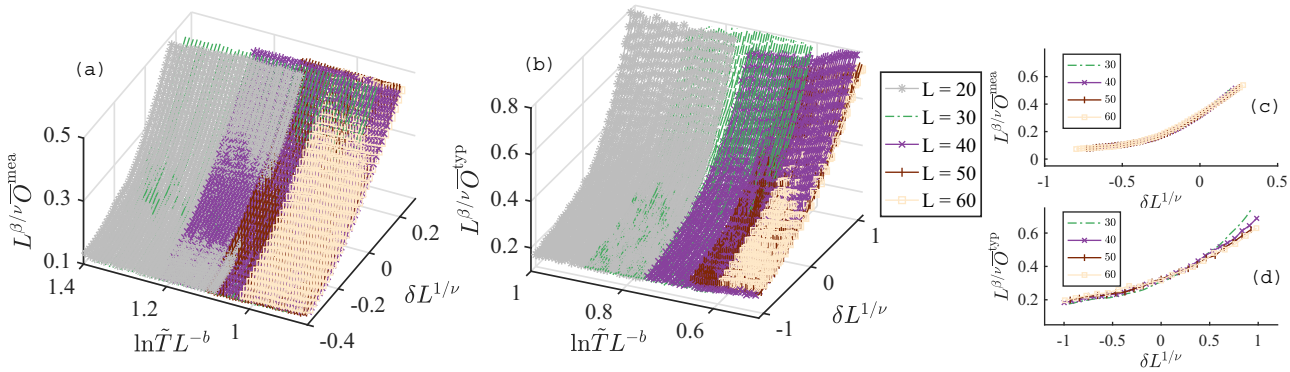

FIG. 6. The finite-time–finite-size scaling of critical dynamics under random initial states. The scaling function equation (8) is used. (a) The collapsed surface for mean coarse-grained correlations. The fitting yields $\beta = 0.37 \pm 0.14$, $b = 0.43 \pm 0.29$, and $T_0 = 2.09 \pm 0.38$. (b) The collapsed surface for typical correlations with $\beta = 0.49 \pm 0.04$, $b = 0.579 \pm 0.006$, and $T_0 = 1.45 \pm 0.06$. The values of ν exponents are taken from Fig. 2. We choose $L_t = 10$ for coarse-grained correlations. (c) and (d) We choose $\ln\tilde{T}L^{-b} \in [0.932, 0.938]$ (c) and $\ln\tilde{T}L^{-b} \in [0.590, 0.602]$ (d) for mean and typical dynamics, respectively, to show the cross sections of the collapsed surfaces. The collapsed curves confirm the quality of the fitting.

1(b)]. The dynamics for the paramagnetic phase have a similar behavior to that shown in Figs. 1(a) and 1(b) where the correlation undergoes swift oscillations and decays to zero. Comparing the critical dynamics ($g = 0.9$) with $g = 0.8$ or $g = 0.93$, CSD can still be observed in both mean and typical coarse-grained correlations.

Furthermore, we verify the scaling function equation (8) for random initial states. We simulate five system sizes ranging from $L = 20$ to $L = 60$. For each disorder configuration, we choose a random product state as the initial state and perform disorder averaging for the dynamics. As shown in Figs. 6(a) and 6(b), for both mean and typical dynamics, the numerical data collapse onto a single curved surface, which is verified by the cross sections shown in Figs. 6(c) and 6(d). The critical exponents derived from this fitting are consistent with the results in the main text. Especially, critical exponent $b = 0.43 \pm 0.29$ for the mean value, and $b = 0.579 \pm 0.006$ for the typical value. Thus subexponential critical slowing-down holds for a random initial state.

[1] P. A. Lee, N. Nagaosa, and X.-G. Wen, Rev. Mod. Phys. **78**, 17 (2006).
[2] B. Hartmann, D. Zielke, J. Polzin, T. Sasaki, and J. Müller, Phys. Rev. Lett. **114**, 216403 (2015).
[3] S. Kundu, T. Bar, R. K. Nayak, and B. Bansal, Phys. Rev. Lett. **124**, 095703 (2020).
[4] H. Sun, B. Yang, H.-Y. Wang, Z.-Y. Zhou, G.-X. Su, H.-N. Dai, Z.-S. Yuan, and J.-W. Pan, Nat. Phys. **17**, 990 (2021).
[5] X. Li, X. Luo, S. Wang, K. Xie, X.-P. Liu, H. Hu, Y.-A. Chen, X.-C. Yao, and J.-W. Pan, Science **375**, 528 (2022).
[6] H. Gatfaoui, I. Nagot, and P. de Peretti, in *Systemic Risk Tomography*, edited by M. Billio, L. Pelizzon, and R. Savona (Elsevier, New York, 2017), pp. 73–93.
[7] M. Pirani and S. Jafarpour, arXiv:2208.03881.
[8] P. C. Hohenberg and B. I. Halperin, Rev. Mod. Phys. **49**, 435 (1977).
[9] L. Van Hove, Phys. Rev. **95**, 1374 (1954).
[10] L. Landau and I. Khalatnikov, Dokl. Akad. Nauk SSSR **96**, 469 (1954).
[11] R. A. Ferrell, N. Menyhárd, H. Schmidt, F. Schwabl, and P. Szépfalusy, Phys. Rev. Lett. **18**, 891 (1967).
[12] B. I. Halperin and P. C. Hohenberg, Phys. Rev. Lett. **19**, 700 (1967).
[13] M. Silvério Soares, J. Kamphorst Leal da Silva, and F. C. SáBarreto, Phys. Rev. B **55**, 1021 (1997).
[14] B. I. Halperin, P. C. Hohenberg, and S.-k. Ma, Phys. Rev. Lett. **29**, 1548 (1972).
[15] R. Vosk and E. Altman, Phys. Rev. Lett. **110**, 067204 (2013).
[16] F. Wilczek, Phys. Rev. Lett. **109**, 160401 (2012).
[17] H. Watanabe and M. Oshikawa, Phys. Rev. Lett. **114**, 251603 (2015).
[18] V. K. Kozin and O. Kyriienko, Phys. Rev. Lett. **123**, 210602 (2019).
[19] V. Khemani, A. Lazarides, R. Moessner, and S. L. Sondhi, Phys. Rev. Lett. **116**, 250401 (2016).
[20] B. Huang, Y.-H. Wu, and W. V. Liu, Phys. Rev. Lett. **120**, 110603 (2018).
[21] J. Zhang, P. W. Hess, A. Kyprianidis, P. Becker, A. Lee, J. Smith, G. Pagano, I.-D. Potirniche, A. C. Potter, A. Vishwanath, N. Y. Yao, and C. Monroe, Nature (London) **543**, 217 (2017).
[22] S. Autti, V. B. Eltsov, and G. E. Volovik, Phys. Rev. Lett. **120**, 215301 (2018).
[23] S. Autti, P. J. Heikkinen, J. T. Mäkinen, G. E. Volovik, V. V. Zavjalov, and V. B. Eltsov, Nat. Mater. **20**, 171 (2021).
[24] J. Smits, L. Liao, H. T. C. Stoof, and P. van der Straten, Phys. Rev. Lett. **121**, 185301 (2018).
[25] X. Yang and Z. Cai, Phys. Rev. Lett. **126**, 020602 (2021).
[26] M. Yue, X. Yang, and Z. Cai, Phys. Rev. B **105**, L100303 (2022).
[27] X. Nie and W. Zheng, Phys. Rev. A **107**, 033311 (2023).
[28] C. W. von Keyserlingk and S. L. Sondhi, Phys. Rev. B **93**, 245146 (2016).
[29] D. S. Fisher, Phys. Rev. Lett. **69**, 534 (1992).
[30] D. S. Fisher, Phys. Rev. B **51**, 6411 (1995).

[31] R. Vosk and E. Altman, Phys. Rev. Lett. **112**, 217204 (2014).
[32] W. Berdanier, M. Kolodrubetz, S. Parameswaran, and R. Vasseur, Proc. Natl. Acad. Sci. USA **115**, 9491 (2018).
[33] A. Lazarides, A. Das, and R. Moessner, Phys. Rev. Lett. **115**, 030402 (2015).
[34] P. Ponte, Z. Papić, F. Huveneers, and D. A. Abanin, Phys. Rev. Lett. **114**, 140401 (2015).
[35] D. A. Abanin, W. De Roeck, and F. Huveneers, Ann. Phys. (Amsterdam) **372**, 1 (2016).
[36] N. Y. Yao, A. C. Potter, I.-D. Potirniche, and A. Vishwanath, Phys. Rev. Lett. **118**, 030401 (2017).
[37] P. Frey and S. Rachel, Sci. Adv. **8**, eabm7652 (2022).
[38] F. F. Assaad and I. F. Herbut, Phys. Rev. X **3**, 031010 (2013).
[39] M. Girardeau, J. Math. Phys. **6**, 1083 (1965).
[40] D. S. Fisher, J. Appl. Phys. **61**, 3672 (1987).
[41] B. Efron, SIAM Rev. **21**, 460 (1979).
[42] M. E. Newman and G. T. Barkema, *Monte Carlo Methods in Statistical Physics* (Clarendon, Oxford, 1999).
[43] B. M. Terhal and D. P. DiVincenzo, Phys. Rev. A **65**, 032325 (2002).
[44] M. Wimmer, ACM Trans. Math. Software **38**, 1 (2012).
[45] P. Xu and T.-S. Deng, Phys. Rev. B **107**, 104301 (2023).